Research Article Vol. 33, No. 20 / 6 Oct 2025 / Optics Express 41791
Optics EXPRESS

High-sensitivity fiber-tip liquid level sensor with welded AuSn nano-film

YUELIANG XIAO, XIN DING, QIAO LIN, MINGXIU WANG, CHENXU LI, CONGMIN LI, JINGYI HOU, YIPING WANG, AND SHEN LIU*

Guangdong and Hong Kong Joint Research Centre for Optical Fiber Sensors, State Key Laboratory of Radio Frequency Heterogeneous Integration, College of Physics and Optoelectronic Engineering, Shenzhen University, Shenzhen 518060, China
*shenliu@szu.edu.cn

Abstract: We proposed a novel method for preparing nanoscale hermetic composite films using AuSn alloy to fabricate a fiber-optic Fabry–Pérot interferometer, developing a liquid-level sensor. The sensor employs a ceramic ferrule integrated fiber-tip with an AuSn alloy composite film, exhibiting high sensitivity for liquid-level measurement and repeatable response for long-term underwater applications. As a result, the sensor's liquid-level sensitivity is measured to ~260 pm/cm, with a liquid-level resolution of ~0.01 cm and a liquid-level measurement range of ~403 cm. The proposed sensor demonstrates significant potential for underwater multi-parameter sensing applications, attributed to its high sensitivity and excellent stability.

1. Introduction

Liquid-level measurement is widely applied in various fields, including oil storage [1], chemical production [2], and fuel storage [3]. Current methods for liquid-level measurement include capacitance [4], magnetostrictive [5], ultrasonic [6], and optical sensing [7]. Despite that electrical-based sensors are widely employed, their applicability is limited when the sensing medium is conductive, potentially explosive and erosive [8]. Fiber-optic sensors have gained significant attention in liquid-level sensing compared to traditional liquid-level monitoring methods [9] due to their strong resistance to electromagnetic interference, high flexibility, and inherent safety [10]. Over the past few decades, various fiber-optic-based liquid-level sensors have been proposed and demonstrated, including Fabry–Pérot interferometer (FPI) [11], Mach–Zehnder interferometer [12], fiber Bragg grating [13], multimode interferometer [14], and tapered fiber [15]. For instance, Jie. Du et al. developed a tilt long-period fiber grating sensor, achieving a high sensitivity of 8.26 nm/mm within the range of 0–16 mm [16]. Joana Martins et al. developed an FPI sensor based on a polyurethane resin film, achieving a sensitivity of 4.4 pm/mm in the large range of 0–9 m [8]. However, polyurethane resins are prone to degradation during prolonged use in humid environments, leading to a decline in sensor performance [17]. Notably, the design of the film material plays a crucial role in determining the FPI liquid-level sensitivity and measurement range. Although the wet transfer technique is a common method for fabricating nano-films, the weak van der Waals force adhesion to the substrate often significantly reduces with increasing temperature [18]. Moreover, the adhesion of these nanofilms to the substrate makes it difficult to meet the demand for hermeticity in liquid-level measurement.

In this paper, we demonstrate a novel method for fabricating nanoscale hermetic composite films based on AuSn alloy film welding and utilize this method to fabricate a thin-film-based fiber-optic FPI liquid-level sensor. Additionally, various aspects of sensors, including reproducibility, hysteresis, and time-domain stability, have been investigated. The results indicate that our proposed liquid-level sensor exhibits a sensitivity of ~260 pm/cm over the liquid-level of ~403 cm, with a resolution of ~0.01 cm, i.e., the pressure sensitivity is ~2.65 nm/kPa, with the pressure range of ~39.5 kPa and pressure resolution of ~0.98 Pa, notably, where there exists a clear

#569196 https://doi.org/10.1364/OE.569196
Journal © 2025 Received 28 May 2025; revised 5 Sep 2025; accepted 15 Sep 2025; published 23 Sep 2025

Optics EXPRESS

corresponding conversion relationship between liquid-level and pressure. According to the liquid pressure formula $p=\rho gh$, where p is the liquid pressure, ρ is the density of the water, g is the acceleration of gravity, and h is the liquid-level height, when the liquid-level height changes by 1 cm, the corresponding pressure changes by ~98 Pa. This unique method of fabricating hermetic nano-films enables the proposed liquid-level sensors to achieve superior performance, which provides promising opportunities for high-precision and wide-range liquid-level applications.

2. Sensor fabrication and principle

Figure 1(a) illustrates the schematic diagram of the proposed fiber-optic FPI liquid-level sensor, which consists of a single-mode fiber (SMF) and a ceramic ferrule with a welded AuSn alloy composite film, which is composed of Cr, Au, and AuSn alloy films, where the lead-in fiber end-face (R_1) and the composite film (R_2) define the FPI cavity. The sensor fabrication involves four steps. In step 1, as shown in Fig. 1(b)–(d), the ceramic ferrule was placed end-face upward in a magnetron sputter coater, sequentially sputtering a Cr film for 1 min, followed by an Au film for 10 mins, and finally, an AuSn film for 24 mins. In step 2, as shown in Fig. 1(e), an Au film is sputtered via magnetron sputter coater sputtering on a polished copper substrate and then transferred to the ferrule end-face to form a complete film. This complete film uses a wet transfer technique, as detailed in Ref. [19]. In step 3, as shown in Fig. 1(f)–(g), an AuSn alloy film was sputtered onto the ferrule end-face and subsequently subjected to hot air gun heating, which facilitated robust interfacial bonding between the wet transferred Au film and the AuSn alloy film, thereby forming a composite film. In step 4, as shown in Fig. 1(h), the SMF insertion depth was precisely controlled using a three-dimensional (3D) displacement platform. Epoxy resin was applied to fix the SMF on the ferrule end-face securely. Using this fabrication method, we successfully fabricated a fiber-optic FPI liquid-level sensor integrated with an ultra-thin composite film with a thickness of hundreds of nanometers.

The light beam propagates to the two inner faces of the FPI cavity. Subsequently, the interference spectral intensity can be described as [20]:

$$I = I_1 + I_2 + 2\sqrt{I_1 I_2}\cos\left(\frac{4n_{eff}L}{\lambda} + \varphi_0\right) \tag{1}$$

where I_1 is the reflected intensity at the end face of the single-mode fiber (R_1), I_2 is the reflected intensity at the inner surface of the composite film (R_2), n_{eff} is the refractive index of the medium in the FPI cavity, where $n_{eff} = 1$ is because the FPI cavity is an air cavity, L is the length of the FPI cavity, λ is the wavelength, and φ_0 is the initial phase. According to Eq. (1), when the condition $4n_{\text{eff}}L/\lambda + \varphi_0 = (2m+1)\pi$ is met, where m is an integer, the interference intensity is minimum. The corresponding interference spectrum at the wavelength can be expressed as [21]:

$$\lambda_r = \frac{4\pi n_{eff}L}{(2m+1)\pi - \varphi_0} \tag{2}$$

the relationship between the dip wavelength shift ($\Delta\lambda_r$) and the cavity length reduction (ΔL) can be expressed as [22]:

$$\frac{\Delta\lambda_r}{\lambda_r} = \frac{\Delta L}{L} \tag{3}$$

Resolution is one of the key parameters for evaluating the liquid-level sensors' performance. It is worth mentioning that the effective resolution of the liquid-level depends on the sensor noise

Optics EXPRESS

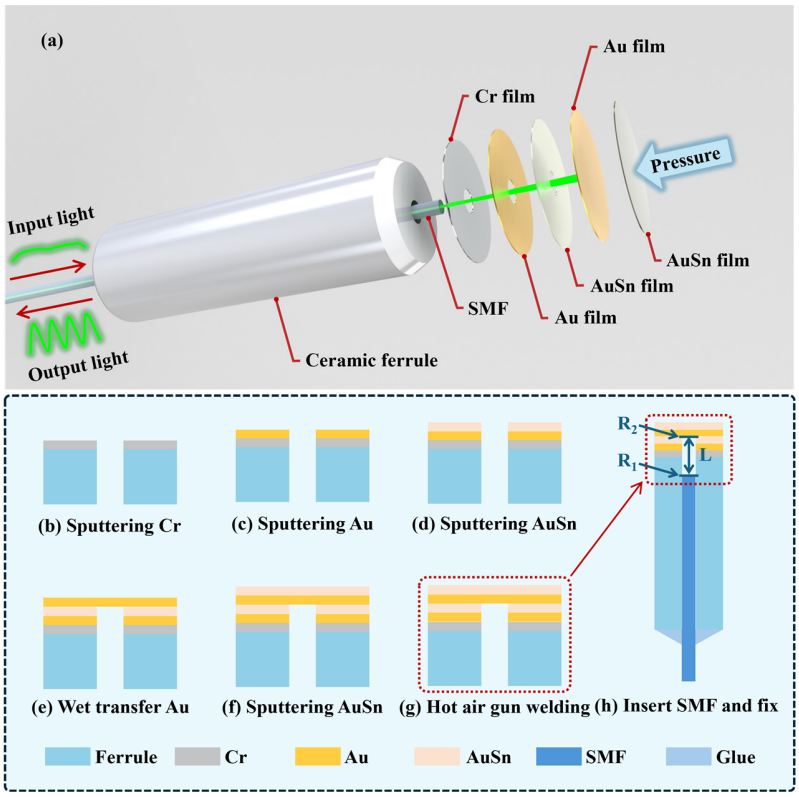

Fig. 1. (a) Exploded view of the sensor. (b)–(d) Cr, Au, and AuSn alloy films were sequentially sputtered onto the end face of the ceramic ferrule. (e) Au film was transferred onto AuSn alloy film via the wet transfer technique. (f) Sputtering of AuSn alloy film onto Au film. (g) Hot air gun welding. (h) Insert the SMF into the ceramic ferrule, which is fixed with epoxy resin adhesive.

and sensitivity. Therefore, the effective liquid-level resolution can be expressed as:

$$R_{FPI} = \frac{\sigma}{S} \tag{4}$$

where σ is the noise of the sensor, and S is the sensitivity of the sensor, therefore, the pressure resolution can be expressed as:

$$R_P = \rho g R_{FPI} \tag{5}$$

where R_P is the pressure resolution of the liquid-level sensor, ρ is the liquid density, and g is the acceleration of gravity, to be 9.8 N/m.

The ferrule end-face was analyzed using scanning electron microscopy (SEM, Phenom Scientific, ProX-G4) to investigate film topography changes further. Figure 2(a) shows that the sputtered Cr, Au, and AuSn alloy multilayer films on the ferrule end-face exhibited a smooth surface topography. It is worth emphasizing that the Cr film can enhance ferrule-Au adhesion [23], while the Au film's good wetting properties facilitate the formation of AuSn intermetallic compounds during welding [24,25]. The generation of this alloying pound significantly enhances the adhesive strength at the ferrule-film interface. As shown in Fig. 2(e), a 1000× SEM image of the central region showed that the sputtered metal film did not adhere properly due to the hollow section at the center, whose aperture diameter is 125 μm. A complete Au film substrate forms a

Optics EXPRESS

reflective surface for the FPI cavity, while Fig. 2(b) illustrates the post-transfer morphological evolution. As shown in Fig. 2(f), a 1000× SEM image of the central region indicated that the film completely covered the hollow region of the ferrule, forming an entirely reflective surface. As shown in Fig. 2(c), re-sputtering the AuSn alloy film onto the ferrule end-face protected the delicate wet transferred Au film. It facilitated the formation of complexes during the welding process, resulting in a composite film with superior airtightness. As shown in Fig. 2(g), a 1000× SEM image of the central region indicated that the film surface was flat and smooth. Finally, Fig. 2(d) shows the surface morphology after welding. Figure 2(h) presents a 1000× SEM image of the central region, indicating no cavitation or voids in the composite film and confirming its structural integrity after welding.

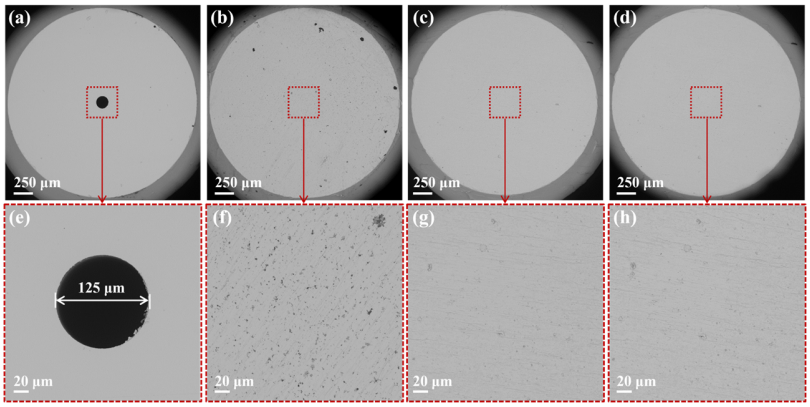

Fig. 2. (a) SEM image of the ferrule end-face after sputtering Cr, Au, and AuSn alloy films. (b) SEM image after the wet transfer of the Au film. (c) SEM image after sputtering the AuSn alloy film. (d) SEM image of (c) after welding. (e)–(h) Show 1000× magnifications of the central regions in (a)–(d), respectively.

The liquid-level sensitivity of the sensor is governed by the thickness of the composite film, where the Au film fabricated by the wet transfer technique and the outermost AuSn alloy film manufactured by sputtering constitute the primary pressure-sensitive components that directly determine the sensor's response to external pressure and thereby its liquid-level sensitivity. To precisely measure the thickness of the Au and Au-AuSn alloy films, a clean Si wafer was positioned adjacent to the sensor as a reference substrate. As shown in Fig. 3(a), a three-step masking process was implemented: (1) A designated area (A1) on the wafers remained uncoated through initial masking; (2) An Au film with sensor-matched thickness was deposited across the wafer except A1, followed by secondary masking to preserve a reference region (A2); (3) The remaining exposed area (A3) received AuSn alloy deposition with sensor equivalent thickness. This stepwise deposition created discrete reference zones (A1: bare Si wafer, A2: Au film, A3: Au-AuSn composite film) for comparative thickness verification through atomic force microscopy (AFM, Seiko Instruments, SPA-300HV). Notice that the Au-AuSn composite film underwent a controlled welding process before the thickness measurement, as illustrated in the thermal profile of Fig. 3(b). Specifically, the AuSn alloy film, whose melting point is 278℃, was heated using a hot air gun at a rate of 25℃/s to 100℃, then at 5℃/s to 280℃, and maintained for 10s to induce partial melting. Subsequently, the temperature was raised at 5℃/s to 320℃ and maintained for 30s. Finally, the heat gun was switched off to allow the structure to cool naturally to room temperature, ensuring complete stabilisation of the welded structure.

Post-welding characterization revealed a distinctly yellowish hue in the composite film, attributed to the interdiffusion between the molten AuSn alloy film and the underlying Au film, which exposed elemental Au at the surface, as illustrated in the insert of Fig. 3(b).

Optics EXPRESS

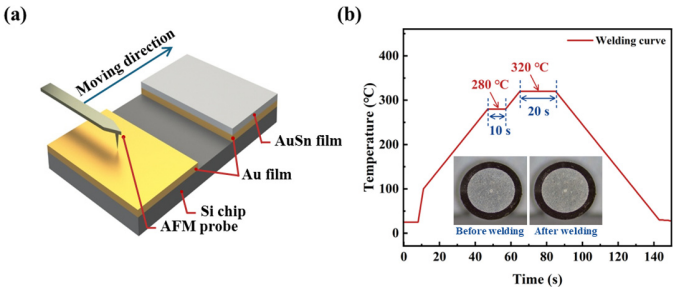

Fig. 3. (a) Schematic illustration of AFM thickness measurement. (b) Welding temperature profile, with insert displaying surface color change post-welding.

After welding, the Au film and the Au-AuSn composite film were measured for thickness using the schematic shown in Fig. 3(a). As shown in Fig. 4(a), the measured Au film thickness is ~44 nm. As shown in Fig. 4(b)–(d), the Au-AuSn film thicknesses for sputtering times of 24 min, 36 min, and 48 min are ~110 nm, ~165 nm, and ~187 nm, respectively, Fig. 4(e)–(h) illustrates the corresponding 3D thickness profiles.

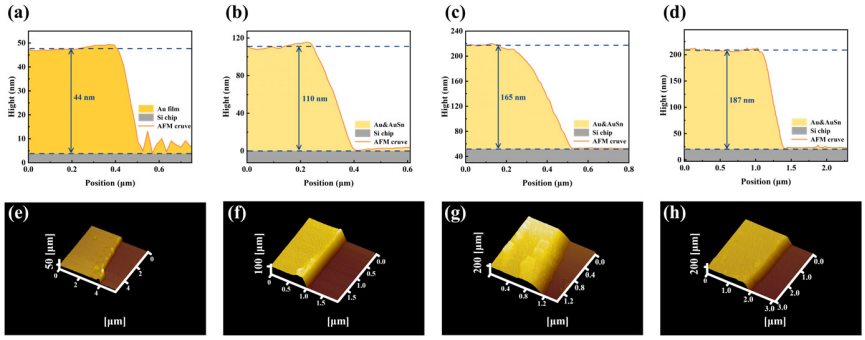

Fig. 4. (a) Thickness of the Au film. (b)–(d) Thickness of the Au-AuSn film formed by welding after sputtering the Au film for 24, 36, and 48 minutes, respectively. (e)–(h) The 3D thickness profile of the Au and AuSn films, respectively.

3. Experiment results and discussion

To investigate the liquid-level response of the proposed sensor, a fiber-optic liquid-level sensing system was developed, as shown in Fig. 5. The sensor was vertically mounted at the bottom of the barrel, and the liquid-level was adjusted by a microfluidic pump (Longer Pump, LSPO2-1B) with a flow rate of 0.5 ml/s, ensuring exceptionally gradual liquid-level changes. Light from a broadband source (BBS, Fiberlake, ASE-EB-D) was directed into the sensor, and reflectance spectra were collected using an optical spectrum analyzer (OSA, Yokogawa, AQ6317C), enabling liquid-level changes to be determined from the dip wavelength shift. The liquid-level can be determined by monitoring the dip wavelength shift in the spectrum, as shown in Eq. (3). The optical switch is adjusted to channel 2 for dynamic response measurement. A tunable laser (TL, New Focus, TLB-6728-P) was inserted at a selected wavelength into the sensor. The optical signal is then received by a photodetector (PD, Thorlabs, PAD05CF2) and transmitted to the computer by the oscilloscope (OSC, Pico Scope, 5244D) for analysis.

To characterize the performance of the proposed sensor in liquid-level measurement, an experiment was conducted using the setup in Fig. 5. As shown in Fig. 6(a), the liquid-level

Optics EXPRESS

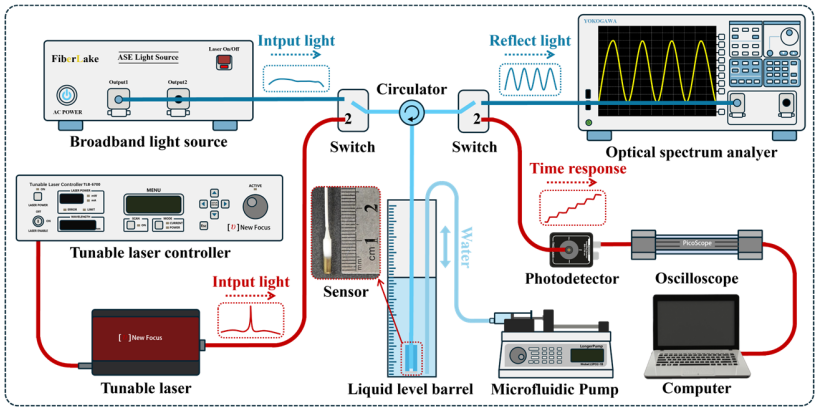

Fig. 5. Experimental setup for fiber-optic liquid-level sensing system.

response characteristics of FP sensor-2, which was fabricated using the proposed method, with a composite film thickness of 165 nm, a free spectral range (FSR) of ~15.77 nm, and an extinction ratio (ER) of ~18.8 dB. The evolution of the reflection spectrum was recorded at room temperature as the liquid-level increased from 2 cm to 20 cm in 2 cm increments. with 5 mins stabilization intervals between measurements to ensure liquid-level stabilization. A blue shift of the dip wavelength was observed with an increasing liquid-level, attributed to hydrostatic pressure-induced compression of the composite film that reduces the FPI cavity length.

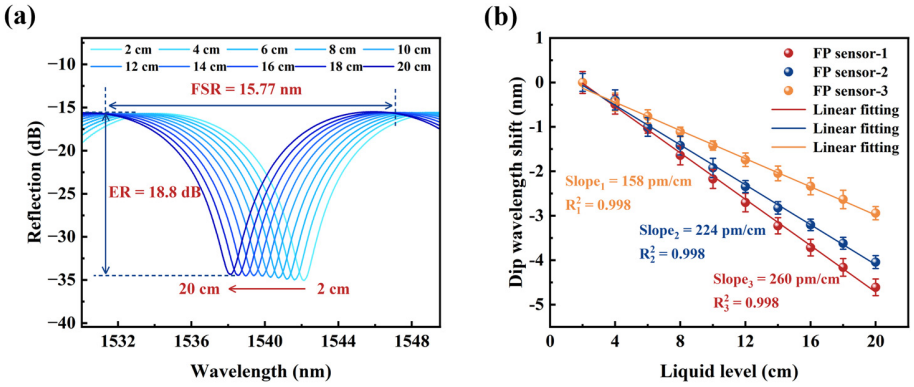

Fig. 6. (a) Reflectance spectral evolution of FPI liquid-level sensor. (b) Dip wavelength shift with different thicknesses during the liquid-level increase.

Three sensors with controlled composite film thicknesses, specifically ~110 nm, ~165 nm, and ~187 nm, were fabricated through precise adjustment of AuSn alloy film sputtering duration time, specifically 24 mins, 36 mins, and 48 mins, thus optimizing the liquid-level sensitivity. Figure 6(b) shows a comparative sensitivity analysis across the 2–20 cm liquid-level range, revealing thickness-dependent performance characteristics: Sensors with a composite film thickness of ~110 nm, ~165 nm, and ~187 nm demonstrated respective sensitivities of ~260 pm/cm, ~224 pm/cm, and ~158 pm/cm, error bars derived from triplicate experimental trials confirm measurement reproducibility, with linear regression analysis yielding R^2 values exceeding 0.998 in three cases. It indicates that the sensor has an excellent linear liquid-level response, and the thinner the composite film, the higher the sensor's sensitivity. What's more, based on this variable thickness film preparation method, the sensitivity and range of the sensor can be

Optics EXPRESS

flexibly varied to meet the needs of different applications. We chose FP sensor-2 (165 nm) for the subsequent liquid-level experiment, which is a compromise between range and sensitivity [26].

The hysteresis analysis in Fig. 7(a) demonstrates a sensitivity discrepancy between the liquid-level increase and decrease phases for the FP sensor-2. Specifically, the sensor exhibited differential sensitivities of ~224 pm/cm increase versus ~214 pm/cm decrease, resulting in a 4.0% hysteresis error attributed to the material's elastic properties. The error resulting from hysteresis directly impacts measurement accuracy, the proposed sensors exhibit low hysteresis error, facilitating the measurement of dynamic liquid-level variations

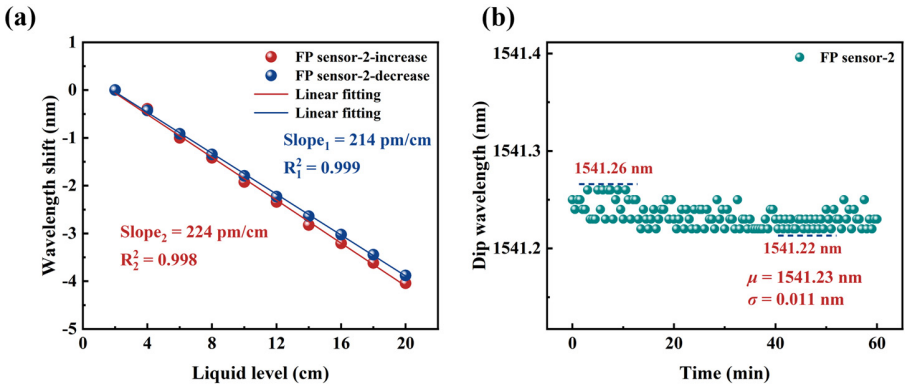

Fig. 7. (a) Dip wavelength shifts during liquid-level increase and decrease. (b) Dip wavelength fluctuation within 60 mins of continuous measurement.

The reproducibility of the FP sensor-2 was evaluated through continuous monitoring of dip wavelength variations at a 5 cm liquid-level over 60 mins with 20 s intervals. As shown in Fig. 7(b), the sensor demonstrated outstanding spectral stability with a mean dip wavelength of ~1541.23 nm, exhibiting a maximum variation of ~0.04 nm, a standard deviation of ~0.011 nm, and a liquid-level detection error limited to ~0.09 mm, equivalent to ~0.88 Pa pressure; the resolution of sensors refers to the most minor dip wavelength shift that can be precisely detected. Based on wavelength demodulation, with an OSA resolution of 0.02 nm and a liquid-level sensitivity of ~260 pm/cm, the liquid-level resolution was determined to be ~0.07 cm, which is equivalent to ~6.8 Pa pressure resolution. Higher resolution enables detection of larger minimal liquid-level variations, the proposed sensors exhibit high liquid-level resolution, making it particularly well-suited for measuring minute variations in liquid-level.

As shown in Fig. 8, a high-level range of ~403 cm, which is equivalent to ~39.5 kPa, was obtained by placing the sensor in a pipe to test the level range of the sensor, with a sensitivity of ~175 pm/cm at ~220 cm before the sensor localised rupture. Additionally, we tested the ranges of other sensors: the 88 nm thickness sensor can withstand a liquid-level of 120 cm, while the 110 nm thickness sensor can withstand a liquid-level of 180 cm. When the pressure on the sensor film exceeds a threshold, the film will undergo localized ruptures, allowing liquid to penetrate into the air cavity, resulting in an inability to maintain the regular wavelength shift. Combined with the resolution of the OSA, a full-scale resolution of ~0.017% can be calculated.

The sensor's dynamic response was measured using the setup in channel 2 of Fig. 5, where the TL couples light at 1548.57 nm into the sensor. The PD converts the optical signals to electrical signals and uses the OSC to capture the electrical signals at a sampling rate of 2000 Hz. During the experiment, the microfluidic pump controlled the liquid-level to rise from 2 mm to 14 mm at 2 mm intervals with an injection time of 3.9 s, and after injection, it was held for 15 s to test the liquid-level stability. As shown in Fig. 9(a), the OSC captures a stepped voltage response with a

Optics EXPRESS

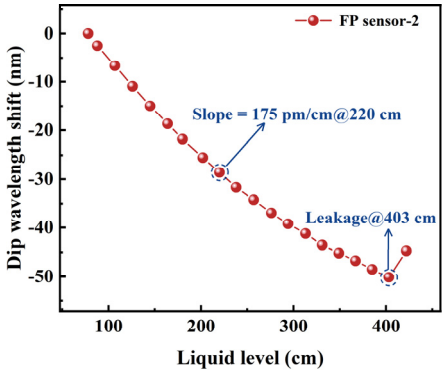

Fig. 8. Liquid-level measurement range experiment.

stable high and low rise and fall. Figure 9(b) shows a zoomed-in graph of the response curve between 50 s and 65 s, with a maximum voltage fluctuation of 0.4 mV.

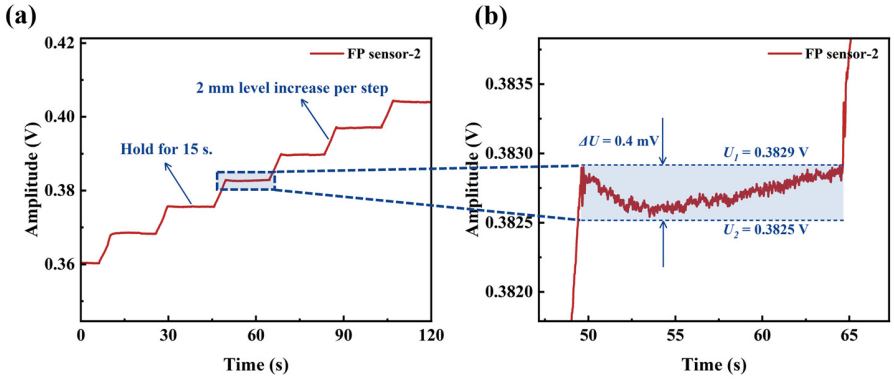

Fig. 9. (a) Output amplitude varies with liquid-level. (b) Local enlarged detail view of (a).

Figure 10 shows the variation of the voltage intensity versus the sensor at different liquid-level heights. After linear fitting, the liquid-level sensitivity was calculated to ~3.62 mV/mm. Based on intensity demodulation, the liquid-level sensor steady-state fluctuation is 0.4 mV, and we can calculate the effective resolution of the system's liquid-level from Eq. (4) as ~0.01 cm, as shown in Eq. (5), equivalent to 0.98 Pa pressure resolution.

The SEM image of the sensor before and after the large-range experiments exhibited a smooth morphology pre-experiment, as shown in Fig. 11(a) and enlarged Fig. 11(b). The localized ruptures of the film occurred, as shown in Fig. 11(c) and enlarged Fig. 11(d), which is due to excessive external pressure exceeding its threshold pressure. Meanwhile, liquid will infiltrate into the cavity, changing the refractive index inside the cavity, this means that the sensor has been damaged and cannot measure accurately. In conclusion, these experimental results demonstrate the sensor's exceptional performance characteristics, including a broad measurement range, high sensitivity, excellent repeatability, and stability suitable for practical applications.

The temperature cross-sensitivity of the liquid-level sensing system is monitored. The sensor was placed into a water bath cylinder, and we gradually increased the temperature from 25℃ to 60℃ at 5℃ and held for 15 mins. The evolution of the dip wavelength as the temperature increases is shown in Fig. 12(a). The dip wavelength was observed to be a red shift with increasing temperatures. The wavelength red shift caused by temperature increase is due to the thermal

Optics EXPRESS

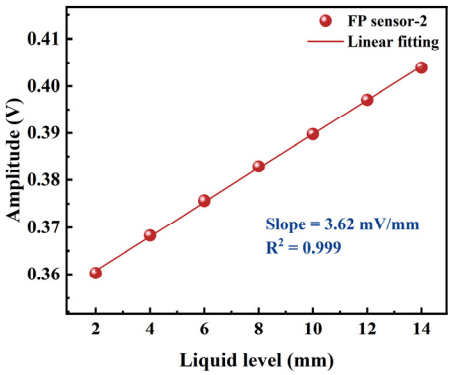

Fig. 10. Variation of amplitude with liquid-level increase.

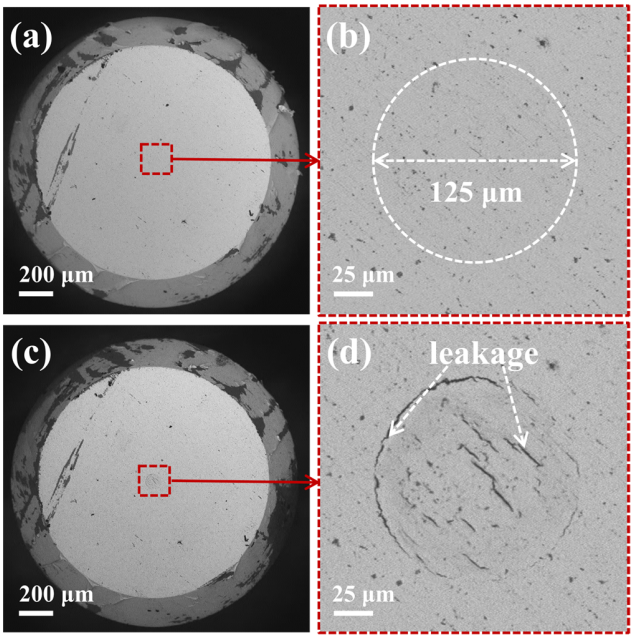

Fig. 11. (a) SEM image of the sensor before immersion. (b) Enlarged view of the central area of (a). (c) SEM image of the sensor after leakage. (d) Enlarged view of the central area of (c).

expansion of air within the enclosed cavity, which increases the cavity length. As shown in Fig. 12(b), the results of the dip wavelength versus temperature relationship, which show 0.18 nm/°C of temperature, the R^2 of the linear fitting is calculated to be 0.999, and the liquid-level sensitivity caused by the equivalent temperature is 0.69 cm/°C. However, our liquid-level sensing experiments are carried out in an ultra-clean room with a constant temperature and humidity, and the temperature fluctuation is less than ±0.05°C in the liquid-level measurement period, so the effects of the temperature fluctuation are ±0.03 cm to the sensor. To further minimize the impact of temperature on liquid-level measurement, the temperature cross-sensitivity of FPI liquid-level sensors can be compensated by FBG (full range) [27,28].

Table 1 summarizes the performance comparison of some optical liquid-level sensors in reference, which shows that the liquid-level measurement using long-period fiber grating has

Optics EXPRESS

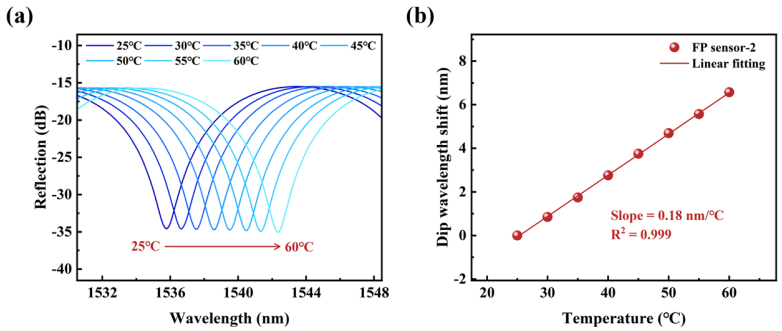

Fig. 12. (a) Reflectance spectral evolution of FPI liquid-level sensor. (b) Dip wavelength shift during temperature increase.

high sensitivity but low range. The FPI liquid-level sensor using polyurethane resins has low sensitivity but wide range. The sensor we proposed can achieve high-sensitivity liquid-level measurement while maintaining a wide measuring range.

Table 1. Performance comparison of the reported liquid-level sensors

Sensor structure	liquid-level sensitivity	Liquid-level range	References
U-shaped cascade fiber	505.4 pm/mm	20 mm	[9]
Fibre Bragg grating	27 pm/mm	300 mm	[13]
Multimode interferometer	154 pm/mm	8 mm	[14]
Long-period fiber grating	8260 pm/mm	16 mm	[16]
Fabry–Pérot interferometer	4.4 pm/mm	9000 mm	[8]
Fabry–Pérot interferometer	26 pm/mm	4030 mm	This work

4. Conclusions

In summary, we proposed a method to fabricate a composite film by welding an AuSn alloy film and successfully utilized the method to design and manufacture a hermetic fiber-optic FPI liquid-level sensor. The proposed method can effectively control the film thickness, improve the underwater measurement performance of the sensor, and make the sensor suitable for more application environments. Fiber-optic FPI liquid-level sensors were fabricated using this fabrication method with good spectral characteristics and a high ER of ~18.8 dB. The sensing performance of the sensor was tested, and the experiment results show that the sensor achieves a sensitivity of ~260 pm/cm, a measurement range of ~403 cm, and a level resolution of ~0.01 mm. These qualities make the sensor provide opportunities for high-precision, wide-range underwater applications.

Funding. National Key Research and Development Program of China (2023YFB3209500); National Natural Science Foundation of China (62422511); Guangdong Science and Technology Department (2023TQ07Z200); LingChuang Research Project of China National Nuclear Corporation (CNNC-LCKY-2024-064); China Postdoctoral Science Foundation (2024T170579).

Disclosures. The authors declare no conflicts of interest.

Data availability. Data underlying the results presented in this paper are not publicly available at this time but may be obtained from the authors upon reasonable request.

References

1. Q. Liu, T. Liu, T. He, *et al.*, "High resolution and large sensing range liquid level measurement using phase-sensitive optic distributed sensor," Opt. Express **29**(8), 11538–11547 (2021).

Optics EXPRESS

2. J. E. Antonio-Lopez, J. J. Sanchez-Mondragon, P. LiKamWa, *et al.*, "Fiber-optic sensor for liquid level measurement," Opt. Lett. **36**(17), 3425–3427 (2011).
3. C. A. R. Diaz, A. Leal-Junior, C. Marques, *et al.*, "Optical Fiber Sensing for Sub-Millimeter Liquid-Level Monitoring: A Review," IEEE Sens. J. **19**(17), 7179–7191 (2019).
4. J. Yu, H. Yu, D. Li, *et al.*, "Design and Characteristic Analysis of Cross-Capacitance Fuel-Level Sensor," Sensors **18**(11), 3984–3993 (2018).
5. Z. Wang, "Design of Magnetostrictive Level Sensor Circuit Based on FPGA," J. Electron Res. Appl. **1**(3), 18 (2017).
6. H. Kim, B. Balagopal, S. Kerrigan, *et al.*, "Noninvasive liquid level sensing with laser generated ultrasonic waves," Ultrasonics **130**, 106926 (2023).
7. J. Wang, Q. Sun, Y. Li, *et al.*, "Highly sensitive liquid-level sensor based on an optical reflective microfiber probe," Opt. Lett. **45**(1), 169–172 (2020).
8. J. Martins, C. A. R. Diaz, M. Fatima Domingues, *et al.*, "Low-Cost and High-Performance Optical Fiber-Based Sensor for Liquid Level Monitoring," IEEE Sens. J. **19**(13), 4882–4888 (2019).
9. M. Wang, Z. Tong, W. Zhang, *et al.*, "Temperature-insensitive liquid level sensor based on a U-shaped cascade core-offset structure," Appl. Opt. **64**(1), 115–122 (2025).
10. K. Liao, Y. Li, M. Lei, *et al.*, "A liquid level sensor based on spiral macro-bending plastic optical fiber," Opt. Fiber Technol. **70**, 102874 (2022).
11. M. Li, S. Wang, J. Jiang, *et al.*, "Cryogen adaptive and integrated differential pressure sensor for level sensing based on an optical Fabry-Perot interferometer," Appl. Opt. **59**(8), 2457–2461 (2020).
12. Y. Yao, J. Yuan, Z. Zhao, *et al.*, "High-resolution liquid level sensor utilizing a microwave photonics interrogated multicore fiber interferometer," Opt. Lett. **48**(23), 6128–6131 (2023).
13. M. Consales, S. Principe, A. Iele, *et al.*, "A Fiber Bragg Grating Liquid Level Sensor Based on the Archimedes' Law of Buoyancy," J. Lightwave Technol. **36**(20), 4936–4941 (2018).
14. J. Li, Q. He, Z. Chen, *et al.*, "Simultaneous measurement of three parameters based on an up-tapered fiber cascaded with a droplet-like multimode interferometer," OSA Continuum **2**(4), 1113–1125 (2019).
15. Y. Li, Z. Song, J. Pan, *et al.*, "In-line reflected fiber sensor for simultaneous measurement of temperature and liquid level based on tapered few-mode fiber," Opt. Express **30**(5), 7870–7882 (2022).
16. J. Du, Z. Gu, Q. Ling, *et al.*, "Design of an anti-temperature interference liquid level sensor based on tilt long-period fiber grating," Opt. Laser Technol. **177**, 111229 (2024).
17. F. Xie, T. Zhang, P. Bryant, *et al.*, "Degradation and stabilization of polyurethane elastomers," Prog. Polym. Sci. **90**, 211–268 (2019).
18. R. C. Batra, M. Porfiri, D. Spinello, *et al.*, "Effects of van der Waals Force and Thermal Stresses on Pull-in Instability of Clamped Rectangular Microplates," Sensors **8**(2), 1048–1069 (2008).
19. J. Luo, "Fiber optic hydrogen sensor based on a Fabry–Perot interferometer with a fiber Bragg grating and a nanofilm," Lab Chip **21**(9), 1752–1758 (2021).
20. X. Wei, X. Song, C. Li, *et al.*, "Optical fiber gas pressure sensor based on polydimethylsiloxane microcavity," J. Lightwave Technol. **39**(9), 2988–2993 (2021).
21. Q. Ma, L. Li, F. Wei, *et al.*, "High sensitivity sensors based on open cavity in fiber Fabry–Pérot and Mach–Zehnder interferometers," J. Opt. Technol. **88**(1), 37–41 (2021).
22. M. Zou, C. Liao, S. Liu, *et al.*, "Fiber-tip polymer clamped-beam probe for high-sensitivity nanoforce measurements," Light: Sci. Appl. **10**(1), 171–178 (2021).
23. C.-C. Chen and F. C.-N. Hong, "Interfacial studies for improving the adhesion of diamond-like carbon films on steel," Appl. Surf. Sci. **243**(1-4), 296–303 (2005).
24. Y. T. Lai and C. Y. Liu, "Study of wetting reaction between eutectic AuSn and Au foil," J. Electron. Mater. **35**(1), 28–34 (2006).
25. L. Yin, S. J. Meschter, T. J. Singler, *et al.*, "Wetting in the Au–Sn System," Acta Mater. **52**(10), 2873–2888 (2004).
26. Y. Chen, Y. Zheng, D. Liang, *et al.*, "Fiber-Tip Fabry–Perot Cavity Pressure Sensor With UV-Curable Polymer Film Based on Suspension Curing Method," IEEE Sens. J. **22**(7), 6651–6660 (2022).
27. M. Chen, D. Yuan, M. Yang, *et al.*, "Two-photon 3D printing FP microcavity sensor for simultaneous measurement of temperature and non-contact pressure," Opt. Laser Technol. **90**, 211–215 (2017).
28. B. Liu, J. Luo, S. Liu, *et al.*, "A Probe-Shaped Sensor with FBG and Fiber-Tip Bubble for Pressure and Temperature Sensing," Photonics Sens. **11**(4), 411–417 (2021).